RSC Advances

PAPER

View Article Online
View Journal | View Issue

Cite this: *RSC Adv.*, 2026, **16**, 3623

pH-dependent redox hydrogen pump for electrochemical direct air capture of CO_2

Xiangyu Zhang,[ab] Yun Zhao, *[a] Yangkai Han,[ab] Zhiwei Ren,[ab] Tao Wei,[ab] Riyang Huang[ab] and Zhigang Shao *[a]

Received 2nd December 2025
Accepted 5th January 2026

DOI: 10.1039/d5ra09310d

rsc.li/rsc-advances

Redox-mediated electrochemical DAC offers a promising, energy-efficient alternative to conventional thermal methods but faces challenges with the oxidative degradation of organic redox mediators in air. While multi-electrolyzer systems mitigate oxygen exposure and solvent loss, the use of common pH-independent redox limits further voltage reductions. To overcome the voltage limitation of pH-independent mediators in electrochemical DAC, this study introduces a new electrochemical DAC strategy utilizing a pH-dependent redox mediator, anthraquinone-2,7-disulfonic acid salt (AQDS), within a dual-electrolyzer system coupled with a hydrogen pump. The pH-dependent redox potential of AQDS lowers the electrolyzer voltage, enabling an actual energy consumption of 257 kJ mol^{-1} CO_2.

1 Introduction

Rising atmospheric concentrations of carbon dioxide (CO_2), a major greenhouse gas, intensify its trapping of long-wave radiation, driving global warming and climate change.[1–3] Direct Air Capture (DAC) is a vital decarbonization strategy that removes low-concentration CO_2 directly from the atmosphere, offering key advantages over flue gas capture such as flexible scalability and minimal geographical constraints.[4,5] Conventional DAC technologies, typically utilizing solid sorbents (*e.g.*, metal–organic frameworks, solid amines, alkali-based sorbents) or alkaline solutions, suffer from significant energy demands during sorbent/solution regeneration and potential secondary pollution.[6–10] In contrast, electrochemical CO_2 capture technologies provide benefits including low energy consumption, simple equipment, and adaptable system size.[11] As electrification advances, electrochemically driven CO_2 capture operating under ambient conditions emerges as a highly attractive solution.

The fundamental principle of electrochemical DAC involves modulating sorbent CO_2 affinity electrochemically to enable reversible CO_2 adsorption/desorption.[11] Recent studies indicate that incorporating redox-active organic molecules can significantly reduce the energy required for electrochemical CO_2 capture and release.[12–14] These strategies primarily utilize two classes of redox-active molecules: (1) proton-responsive molecules, which facilitate CO_2 capture under alkaline conditions or release under acidic conditions by inducing pH shifts through water dissociation;[13–15] and (2) direct CO_2-binding molecules: in their reduced state, these molecules react directly with CO_2, and release the captured CO_2 upon oxidation.[16,17] However, the reduced forms of these organics, often containing amino or hydroxyl groups, are susceptible to O_2-induced oxidative degradation.[14,18] Furthermore, the volatility of the organic solvents/co-solvents employed complicates operation through solvent loss.[16,19]

To mitigate O_2 exposure and solvent evaporation, multi-electrolyzer designs have been adopted and proven effective for both CO_2 capture and reactive capture processes.[20,21] These systems leverage the inherent O_2 tolerance of inorganic CO_2 absorbents while utilizing organic redox mediators to maintain high reaction rates. Nonetheless, a key limitation persists: the pH-independent redox potentials of commonly used mediators restrict the achievable minimization of electrolyzer voltage, whose theoretical voltage is defined as the potential difference between the hydrogen oxidation reaction (HOR) and hydrogen evolution reaction (HER). One pathway to overcome this constraint is by selecting mediators with pH-dependent redox potentials. Quinone compounds represent promising pH-dependent redox with favorable electrochemical properties,[22] yet their application in multi-electrolyzer DAC systems remains unexplored.

Herein, we propose a DAC strategy employing a pH-dependent redox within a dual-electrolyzer system coupled with a hydrogen pump. This configuration utilizes HER to generate OH^- for CO_2 capture and the HOR to produce H^+ for CO_2 release. We selected anthraquinone-2,7-disulfonic acid salt (AQDS) as the redox mediator due to its high reversibility, solubility, and low cost. Crucially, its pH-dependent redox potential enables electrolyte pH modulation, significantly reducing electrolyzer voltage. Using this approach, we achieved direct CO_2 capture from ambient air with an actual energy consumption of 257 kJ mol^{-1} CO_2 at 40 mA cm^{-2}.

---

[a] Fuel Cell System and Engineering Laboratory, Key Laboratory of Fuel Cells & Hybrid Power Sources, Dalian Institute of Chemical Physics, Chinese Academy of Sciences, Dalian 116023, China. E-mail: yunzhao@dicp.ac.cn; zhgshao@dicp.ac.cn

[b] University of Chinese Academy of Sciences, Beijing 100049, China

2 Experimental

2.1 Electrochemical measurements

All electrochemical measurements were conducted at ambient conditions. No *iR* compensation was applied in the electrochemical tests.

Cyclic voltammetry (CV) was performed using a Gamry Interface 1010E electrochemical workstation. In all three-electrode CV configurations, a glassy carbon electrode (GCE) with a diameter of 3.0 mm was employed as the working electrode. A saturated Ag/AgCl electrode, pre-soaked in a saturated KCl solution, served as the reference electrode, while a platinum wire (0.5 mm × 37 mm) was used as the counter electrode. The scan rate was set at 50 mV s^{-1}.

Linear sweep voltammetry (LSV) was conducted using the same workstation in a single-cell configuration. A saturated Ag/AgCl electrode, similarly pre-soaked in saturated KCl solution, was used as the reference electrode. A platinum-coated nickel felt (1 × 1 cm^2) served as the working electrode, and a 3.0 mm diameter glassy carbon electrode was used as the counter electrode. The LSV was performed at a scan rate of 1 mV s^{-1}. The electrolyte consisted of 50 mL of saturated Li_2CO_3 aqueous solution.

Electrochemical impedance spectroscopy (EIS) was also performed using the Gamry Interface 1010E system. Measurements were carried out in the frequency range of 10 kHz to 1 Hz with an amplitude of 0.5 A.

2.2 Ultraviolet-visible (UV-vis) absorption spectroscopy

Ultraviolet-visible (UV-vis) spectra were recorded using a SHIMADZU UV-2550 spectrophotometer. A 2 M LiCl aqueous solution was used as the reference solvent.

2.3 Scanning electron microscopy (SEM)

The morphology and microstructure of the carbon felt were characterized using a field-emission scanning electron microscope (FE-SEM, JSM-IT300LA).

2.4 Electrolytic cell configuration

A custom three-chamber electrolytic cell with an active area of 5.0 cm^2 was assembled for dual-mode operation (Mode I and Mode II). In Mode I configuration, hydrophobic carbon paper was used in the anode chamber. A Nafion 211 membrane, coated with Pt/C catalyst, separated the anode chamber from the central chamber. A piece of carbon felt was placed in the central chamber and served as a shared electrode. In Mode II configuration, a Nafion 115 membrane separated the cathode chamber from the central chamber. A platinum-coated nickel felt electrode was installed in the cathode chamber. Rubber gaskets ensured liquid-tight sealing throughout the assembly.

At the beginning of each experiment, the Mode II cathode chamber was filled with 20 mL of post-capture solution, while the neutralization reservoir was charged with 20 mL of an AQDS/LiCl aqueous. Prior to applying voltage, the central chamber was purged with N_2 gas for 15 minutes. Both solutions were introduced into their respective chambers from the bottom inlet and circulated back into their reservoirs *via* the top outlet of the cell.

2.5 Calculation of energy consumption and faradaic efficiency

Due to the continuous variation of cell voltage during the electrolyzer operation, the operating energy consumption is calculated using eqn (E1) *via* computer processing.

$$E = \int_0^t UI\mathrm{d}t \tag{E1}$$

where E is the energy consumption (J), U is the voltage (V), I is the current (A) and t is the time (s).

Faradaic efficiency is calculated as the ratio between the actual and theoretical masses of Li_2CO_3 produced. Based on the reaction eqn (E2)–(E6), each mole of AQDS theoretically yields one mole of Li_2CO_3.

In Mode I:

$$\text{Anode: } H_2 - 2e^- \rightarrow 2H^+ \tag{E2}$$

$$\text{Cathode: AQDS} + 2e^- + 2H^+ \rightarrow \text{AQDSH}_2 \tag{E3}$$

In Mode II:

Anode:

$$\text{AQDSH}_2 - 2e^- + Li_2CO_3 \rightarrow \text{AQDS} + CO_2(g) + H_2O + 2Li^+ \tag{E4}$$

$$\text{Cathode: } 2H_2O + 2e^- \rightarrow 2OH^- + H_2 \tag{E5}$$

In DAC

$$2Li^+ + 2OH^- + CO_2 \rightarrow Li_2CO_3(s) + H_2O \tag{E6}$$

Therefore, the faradaic efficiency is determined according to eqn (E7)

$$\text{FE} = \frac{m(Li_2CO_3)}{n(\text{ADQS}) \times M(Li_2CO_3)} \tag{E7}$$

where FE is the faradaic efficiency (%), n(AQDS) is the amount of substance of AQDS (mol), $m(Li_2CO_3)$ is the actual mass of Li_2CO_3 produced (g), and $M(Li_2CO_3)$ is the molecular mass of Li_2CO_3 (73.89 g mol^{-1}).

3 Results and discussion

3.1 Concept and validation of an AQDS-mediated hydrogen pump for DAC cell voltage reduction

To prevent AQDS deactivation by oxygen, we developed an electrochemical strategy coupling a redox pair with a hydrogen pump (Fig. 1). This system simultaneously leverages both the O_2-tolerance of inorganic CO_2 sorbents and exploits the pH-dependent redox potential of the organic mediator.

The system operates alternately in Mode I and Mode II, utilizing a carbon felt electrode in the central compartment that functions as the cathode during Mode I and as the anode during Mode II. Both electrolyzers employ cation exchange membranes

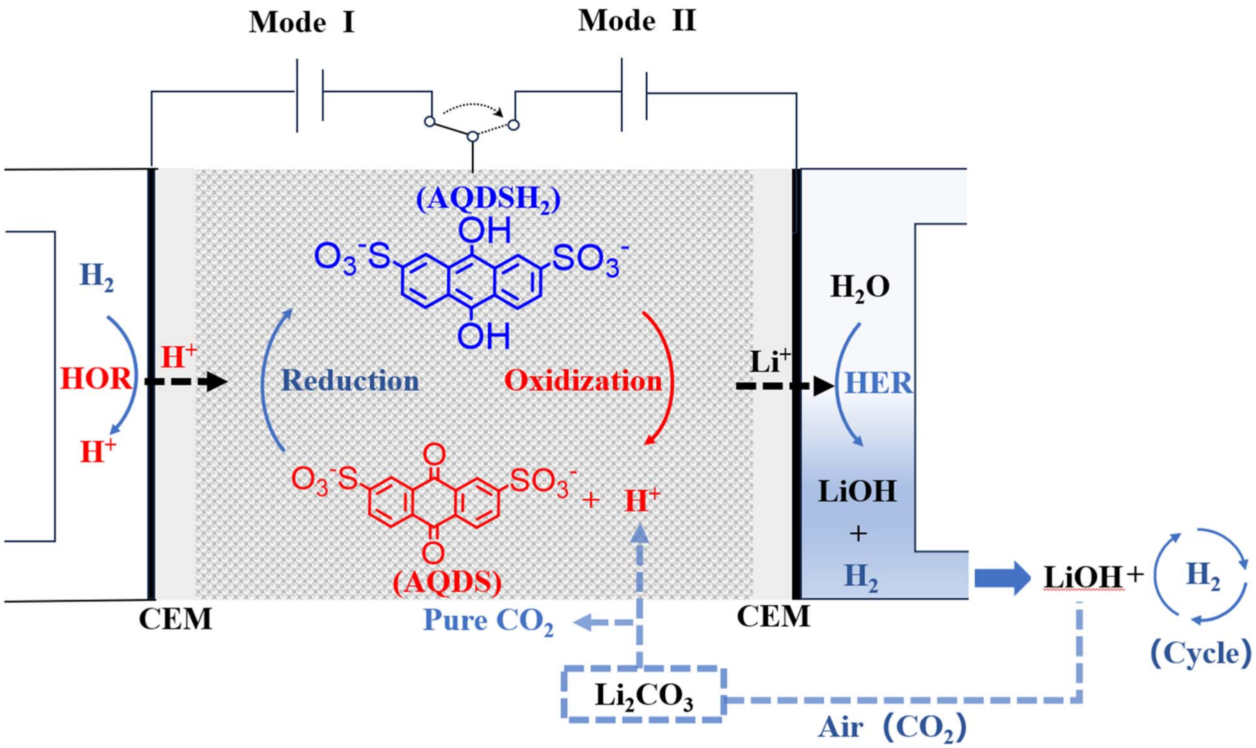

Fig. 1 Schematic of the hydrogen-pump electrolyzer system for AQDS-mediated electrochemical DAC. The three-compartment cell integrates a redox mediator (AQDS) with hydrogen evolution/oxidation reactions. Anode: Pt/C serves as the catalyst for HOR; central chamber: carbon felt used as the electrode for the AQDS redox cycling; cathode: Pt-coated nickel felt electrode employed for HER.

(CEMs) to enable cation migration from anode to cathode (Fig. 1).

In Mode I, the HOR at the anode generates H^+ ions, which migrate through the CEM and react with AQDS at the cathode to form $AQDSH_2$. Following Mode I, Li_2CO_3—formed by atmospheric CO_2 absorption into LiOH solution in Mode II—is introduced, establishing an alkaline environment.

In Mode II, $AQDSH_2$ undergoes oxidation at the anode. The elevated pH (from Li_2CO_3 addition) lowers the AQDS redox potential, reducing the required electrolyzer voltage. Concurrently, generated H^+ protonates carbonate ions (CO_3^{2-}) to release CO_2, while Li^+ migrates to the cathode. HER at the cathode then produces LiOH and H_2, enabling H_2 recycling to the Mode I anode and the LiOH reuse for CO_2 capture.

The theoretical total voltage for Mode I and Mode II operation varies with redox selection (Fig. 2a). Redox couples like I_2/I^- (ref. 21) and $BPPV^{2+}/BPPV^+$ (ref. 20) exhibit pH-independent potential; consequently, their combined voltage equals the thermodynamic HOR/HER potential difference (E_{HOR}–E_{HER}). For example, using $BPPV^{2+}/BPPV^+$, Mode I requires a voltage (ΔE_4) equivalent to the potential gap between HOR and BPPV reduction, while Mode II requires a voltage (ΔE_3) spanning BPPV oxidation to HER. The sum $\Delta E_3 + \Delta E_4$ thus equals E_{HOR}–E_{HER}. In contrast, AQDS/$AQDSH_2$ possesses a pH-dependent redox potential. During Mode I (acidic conditions), its more positive potential narrows the gap to HOR ($\Delta E_6 < \Delta E_4$). During Mode II (alkaline conditions), its more negative potential approaches HER ($\Delta E_5 < \Delta E_3$). This pH-triggered potential shift yields a lower total voltage ($\Delta E_5 + \Delta E_6$), which is strictly less than E_{HOR}–E_{HER}.

To validate this concept, CV measurements of AQDS under varying pH conditions confirm significant potential shifts (Fig. 2c). In 0.2 M HCl (simulating Mode I), AQDS exhibits a redox potential of +0.009 V *vs.* Ag/AgCl. Under 0.2 M Li_2CO_3 (simulating Mode II), the potential cathodically shifts to −0.467 V *vs.* Ag/AgCl—a 476 mV difference. These results demonstrate that acidic and alkaline conditions profoundly modulate the AQDS redox potential, directly enabling the electrolyzer voltage reduction mechanism proposed in Fig. 2a.

3.2 Electrolytic cell performance analysis

We first assessed the performance of each electrolyzer operating at 40 mA cm^{-2}, circulating 20 mL of 0.10 M AQDS solution through the middle chamber at 20 mL min^{-1}. As shown in Fig. 3b, Mode I commenced at a cell voltage of 0.243 V, while Mode II started at 0.624 V. As electrolysis approached completion in both modes, a pronounced increase indicated near-complete consumption of AQDS reactant during reduction (Mode I) and oxidation (Mode II).

Under the experimental conditions, the HOR potential is 0 V *vs.* SHE, while LSV measurements show a HER onset potential of the −0.715 V *vs.* SHE in saturated lithium carbonate solution (E_{HOR}–E_{HER} = 0.715 V). The theoretical voltages for Mode I and Mode II using the I_2/I^- and $BPPV^{2+}/BPPV^+$ redox couples is therefore 0.715 V.

However, due to the lowered AQDS redox potential from the lithium carbonate addition, the theoretical sum for Mode I and II is expected to be below 0.715 V. Experimentally, at 10 mA cm^{-2},

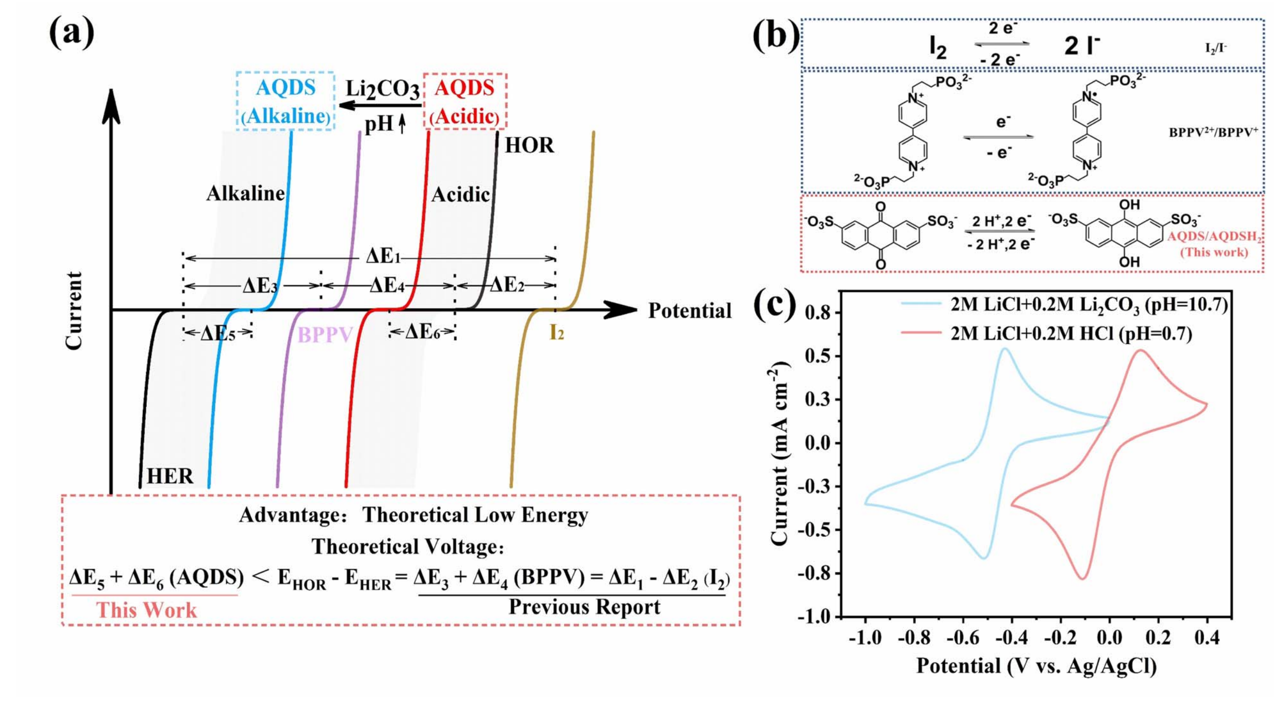

Fig. 2 Voltage reduction in AQDS-mediated electrochemical DAC *via* pH-dependent redox potential. (a) Theoretical operating voltages for Modes I and II using different mediators. For pH-independent mediators (*e.g.*, $BPPV^{2+}/BPPV^{+}$, I_2/I^-), the total voltage equals the thermodynamic HOR–HER potential difference ($\Delta E_{HOR-HER}$). For AQDS/$AQDSH_2$, pH-dependent potential shifts reduce the total voltage below $\Delta E_{HOR-HER}$. (b) Oxidized/reduced states of representative mediators. Only AQDS/$AQDSH_2$ undergoes proton-coupled electron transfer. (c) Cyclic voltammograms of AQDS under simulated Mode I (0.2 M HCl) and Mode II (0.2 M Li_2CO_3) conditions, demonstrating the pH-induced cathodic shift (~59 mV pH^{-1}) that enables voltage reduction.

the sum of the initial onset voltages is indeed lower than 0.715 V (Fig. 3a). Conversely, at higher current densities (40, 70, and 100 mA cm^{-2}), this sum exceeds 0.715 V, attributed to increased ohmic losses. To evaluate these ohmic losses in the Mode I and II electrolyzers, EIS was conducted as shown in Fig. 3c.

UV-vis absorption spectroscopy confirmed AQDS reduction during Mode I operation (Fig. 3d). Oxidized AQDS exhibits a strong peak at 325 nm (attributed to the C═O groups) and a broad, weak peak near 482 nm, potentially arising from Li^+ complexation with C═O oxygen due to the similar ionic radii of Li^+ and H^+. Upon reduction, a new peak emerges at 391 nm, characteristic of O–H groups in $AQDSH_2$. The persistence of the 325 nm peak is likely due to incomplete reduction or sample dilution effects during measurements. The disappearance of the 482 nm peak is attributed to decreased solution pH upon AQDS reduction, where increased H^+ concentration outcompetes Li^+ for complexation sites. Furthermore, a visible color change from red to green in the middle chamber during Mode I operation directly confirmed the reduction of AQDS.

To evaluate the DAC potential, the Mode II-regenerated LiOH solution was exposed to ambient laboratory air (CO_2 concentration: 504.2 ± 8.4 ppm) at 200 sccm for ~23 hours (Fig. 3e). The initial catholyte pH in Mode II was 11.09 ± 0.57; after electrochemical regeneration, it increased to 13.16 ± 0.07, confirming strong alkalinity. During DAC, the pH decreased from 13.16 ± 0.07 to 11.09 ± 0.57, consistent with OH^- conversion to CO_3^{2-} upon CO_2 absorption. Centrifugation of the CO_2-loaded solution produced 78.6 ± 8.2 mg of solid Li_2CO_3, corresponding to a CO_2 capture faradaic efficiency of 67%.

Theoretically, Mode I and Mode II should operate for equivalent durations. Experimentally, however, Mode II electrolysis completed 495 seconds faster than Mode I (Fig. 3b). Gas evolution during Mode II operation and solid precipitates observed in post-operation are attributed to partial reaction of reduced AQDS species with CO_2, forming a precipitate. Cyclic voltammograms confirmed significantly reduced AQDS. Cyclic voltammograms confirmed significantly reduced AQDS redox reversibility under CO_2 *versus* N_2 (Fig. 3f). The underlying mechanism involves dissociation of $AQDSH_2$ into H^+ and $AQDS^{2-}$; the H^+ reacts with Li_2CO_3 to liberate CO_2, which then reacts with $AQDS^{2-}$ to form the $AQDS(CO_2)_2^{2-}$ precipitate. This process, described by reactions (1)–(3) in Fig. 4, aligns with literature reports.[12]

3.3 Comparison of energy consumption

The energy consumption for CO_2 capture varies across different systems. For systems where by-products are generated, such as in water electrolysis-based CO_2 capture,[23] the total system energy consumption must be subtracted by the Gibbs free energy of generating the by-products (*e.g.*, hydrogen) to obtain the net energy consumption for CO_2 capture. In this work, under Mode II, the hydrogen generated is consumed by Mode I, resulting in net zero hydrogen production and no other by-products. Consequently, the total system energy consumption

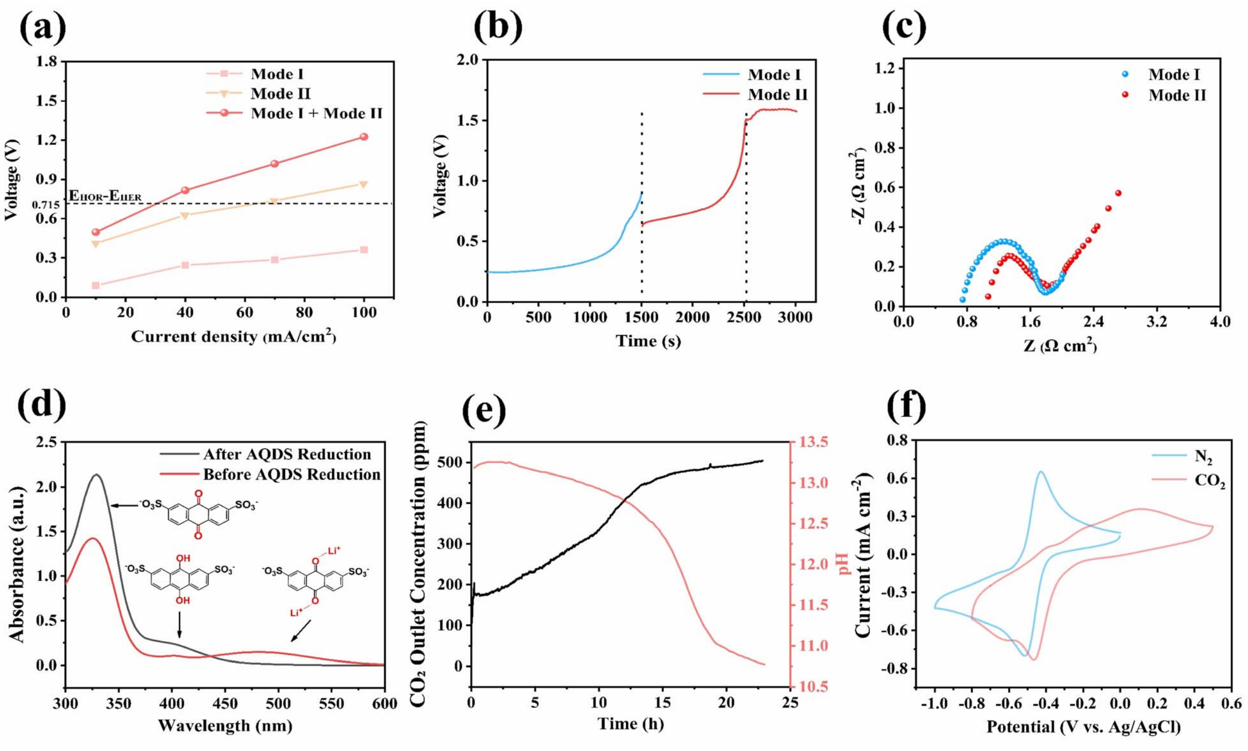

Fig. 3 Electrolytic cell performance of the AQDS-mediated DAC system. (a) Initial operating voltages *vs.* current density for Mode I and II, measured at 10, 40, 70, and 100 mA cm^{-2}. (b) Cell voltage profiles during individual Mode I and Mode II operation at a constant current density of 40 mA cm^{-2} (room temperature; electrode area: 5 cm^2). (c) Nyquist plots at 40 mA cm^{-2} (EIS frequency range: 100 kHz-1 Hz). (d) UV-vis spectra of oxidized and reduced AQDS. (e) Outlet CO_2 concentration and pH evolution during DAC using alkaline solution regenerated *via* Mode II. (f) Cyclic voltammograms of AQDS electrolyte under N_2 *vs.* CO_2 atmospheres.

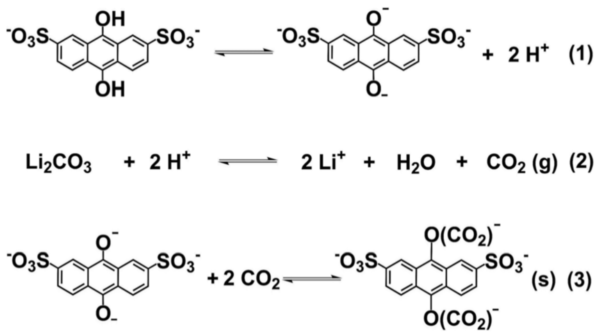

Fig. 4 Reaction equations between $AQDSH_2$ and CO_2. The liberated H^+ then reacts with Li_2CO_3 to release CO_2, which subsequently combines with AQDS^{2-} to form the AQDS(CO2)$_2{}^{2-}$ precipitate.

corresponds directly to the energy required for CO_2 capture. The minimum theoretical energy input for CO_2 capture *via* this AQDS-mediated process is 173 kJ mol^{-1} CO_2, calculated under ideal conditions assuming 100% molecular utilization and no side reactions between reduced AQDS and CO_2. However, under actual operating conditions (40 mA cm^{-2}), unavoidable side reactions with CO_2 cause precipitate formation, increasing the practical energy demand to 257 kJ mol^{-1} CO_2 for the coupled electrolyzer-hydrogen pump system. This corresponds to a practical faradaic efficiency of 67%. Table 1 benchmarks this system against other redox-active DAC molecules, revealing that the our ideal energy consumption is notably lower than previously reported values. We also compare the energy consumption of several common DAC methods. It is evident that the multi-chamber system can significantly reduce operational energy consumption. The comparison further demonstrates that the energy consumption of the this work remains at a relatively low level within this field.

3.4 Electrolytic cell cycling and analysis

We conducted five consecutive Mode I/II cycles at 40 mA cm^{-2} (Fig. 5a). A sharp voltage increase occurred during the second Mode II cycle, attributed to precipitate formation from AQDS-CO_2 reactions depositing onto the carbon felt. This deposit blocked electroactive sites and impeded redox kinetics, as confirmed by post-operation disassembly. After cleaning the carbon felt, normal performance resumed in the third cycle. To assess long-term effect, cycles four and five proceeded without cleaning, leading to rapid performance decay. Filtering the central compartment solution post-cycling collected visible precipitate, confirming *in situ* precipitate formation (Fig. 5b). SEM analysis further substantiated the degradation mechanism: cycled carbon fibers showed extensive coating by solid deposits (Fig. 5d), contrasting sharply with the pristine precycling structure (Fig. 5c). Collectively, these results demonstrate that electrode fouling by precipitates drives the observed electrochemical degradation.

Table 1 Energy consumption comparison of several common DAC/DOC

Type	Mechanism	CO_2 separation work inputs (kJ per mol CO_2)	Current density (mA cm^{-2})	Ref.
Multi-electrolyzer system (using redox active molecules)	This work	173^a 257	40	—
	BPPV alternating electrocatalysis	202^a 220	40	20
	Iodide alternating electrocatalysis	238^a 264	40	21
Multi-electrolyzer system (no redox active molecules)	Porous solid-electrolyte reactor	299	3	24
	Ferricyanide coupled DOC using BPMED	155	3.3	25
	DAC using bipolar membrane electrodialysis (BPMED)	462	8.6	26
Single-electrolyzer systerm	Traditional alkaline sorbent regeneration	458	10	27
	Fuel cell concentrator	809	20	28
	Alkaline sorbent regeneration through anion exchange resin	374	5	29

[a] In the table indicates the faradaic efficiency under ideal conditions (100% molecular utilization).

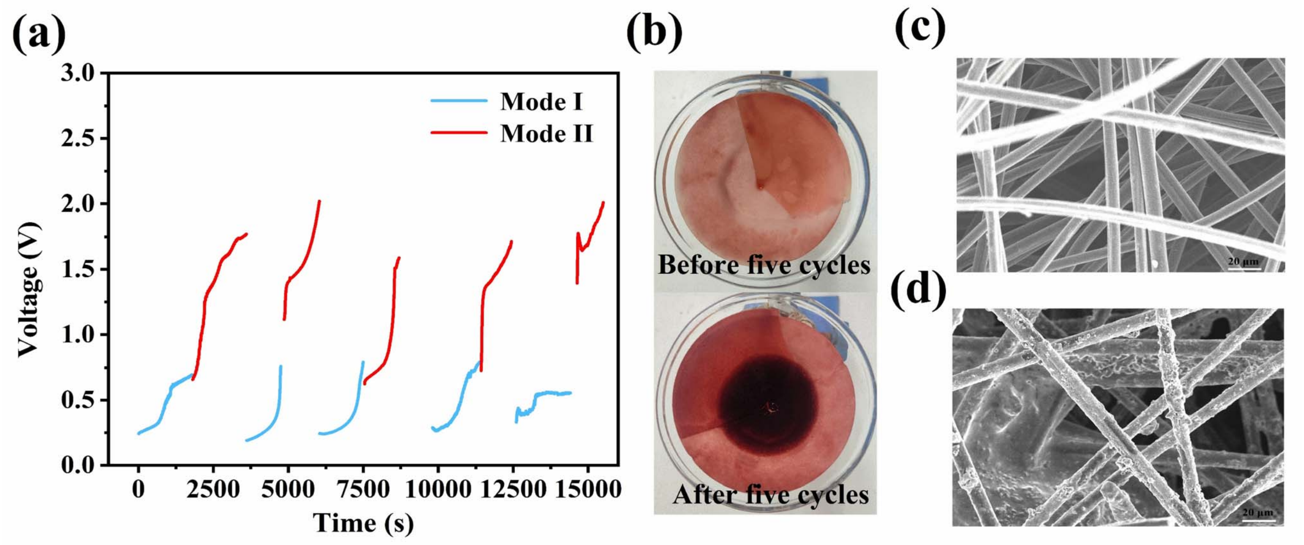

Fig. 5 Cycling Stability. (a) Electrolyzer voltage profiles during five consecutive Mode I/II cycles at 40 mA cm^{-2}. (b) The comparison of filtrating solution the in the central compartment before and after five cycles. (c) SEM image of the carbon felt before five cycles. (d) SEM image of the carbon felt after five cycles.

The precipitated molecules can be regenerated into $AQDSH_2$ by the addition of hydrochloric acid. Upon evaporation of the solvent under ambient air conditions, the AQDS molecules can be recovered for reuse. However, this process involves additional costs and energy consumption. The deactivation of AQDS molecules leading to electrode passivation is a challenge specific to AQDS molecules, and quinone compounds in general, rather than an inherent flaw in the overall concept. This issue is addressable and can be effectively mitigated through future molecular design strategies. Therefore, future efforts should focus on developing advanced redox-active molecules that satisfy three key criteria: (i) stability across a wide pH range, (ii) a CO_2-resistant reduced form, and (iii) a pH-tunable redox potential, to enhance the performance and durability of the electrochemical DAC systems.

4 Conclusions

In summary, we developed an electrochemical direct air capture system leveraging oxygen-tolerant hydroxide capture solutions and pH-dependent redox mediators to achieve low-energy CO_2 capture. At 40 mA cm^{-2}, the ideal energy consumption is 173 kJ mol^{-1} CO_2 (100% molecular utilization). In practical operation, however, side reactions between reduced AQDS and CO_2, cause molecular deactivation and precipitate formation, increasing energy demand to 257 kJ mol^{-1} CO_2 and compromising cycling stability. Consequently, molecular design of advanced redox-active compounds emerges as the critical pathway to improve robustness and long-term performance in this DAC approach.

Author contributions

Xiangyu Zhang: writing – original draft, methodology, investigation, data curation, conceptualization. Yun Zhao: writing – review & editing, supervision, funding acquisition, conceptualization. Yangkai Han: investigation, data curation. Zhiwei Ren: investigation. Tao Wei: investigation. Riyang Huang: data curation. Zhigang Shao: supervision.

Conflicts of interest

The authors declare no conflicts of interest.

Data availability

The data that support the findings of this study are available from the corresponding author upon reasonable request.

Supplementary information (SI) is available. See DOI: https://doi.org/10.1039/d5ra09310d.

Acknowledgements

This work was financially supported by National Natural Science Foundation of China (No. 22279134) and LiaoNing Revitalization Talents Program (No. XLYC2203150).

Notes and references

1 J.-L. Dufresne, V. Eymet, C. Crevoisier and J.-Y. Grandpeix, *J. Clim.*, 2020, **33**, 3827–3844.
2 K. Hu, G. Huang, P. Huang, Y. Kosaka and S. P. Xie, *Nat. Geosci.*, 2021, **14**, 377–382.
3 A. Mikhaylov, N. Moiseev, K. Aleshin and T. Burkhardt, *J. Entrep., Sustain. Issues*, 2020, **7**, 2897–2913.
4 G. Li and J. Yao, *Engineering*, 2024, **5**, 1298–1336.
5 J. Wang, R. Fu, S. Wen, P. Ning, M. H. Helal, M. A. Salem, B. B. Xu, Z. M. El-Bahy, M. Huang, Z. Guo, L. Huang and Q. Wang, *Adv. Compos. Hybrid Mater.*, 2022, **5**, 2721–2759.
6 V. Chanal, S. Humpage and M. Millinger, *Environ. Res. Lett.*, 2025, **20**, 044047.
7 B. Francesco, G. Claudia, M. Fabrizio and P. Maurizio, *ACS Sustainable Chem. Eng.*, 2020, **8**, 14013–14021.
8 L. Qiu, N. Mokhtarinori, H. Liu, D. e. Jiang, Z. Yang and S. Dai, *Mater. Today Energy*, 2025, **47**, 101740.
9 C. Radu, *Chem. Sci.*, 2021, **12**, 12518–12528.
10 Q. Sun, J. Xiong, H. Gao, T. Sema, W. Olson and Z. Liang, *Green Chem.*, 2023, **25**, 4647–4655.
11 K. Sun, M. Tebyetekerwa, H. Zhang, X. Zeng, Z. Wang, Z. Xu, T. E. Rufford and X. Zhang, *Adv. Energy Mater.*, 2024, **14**, 2400625.
12 Y. Jing, K. Amini, D. Xi, S. Jin, A. M. Alfaraidi, E. F. Kerr, R. G. Gordon and M. J. Aziz, *ACS Energy Lett.*, 2024, **9**, 3526–3535.
13 L. Luo, L. Hou, Y. Liu, K. Wu, Y. Zhu, H. Lu and B. Liang, *Energy Fuels*, 2021, **35**, 12260–12269.
14 S. Pang, S. Jin, F. Yang, M. Alberts, L. Li, D. Xi, R. G. Gordon, P. Wang, M. J. Aziz and Y. Ji, *Nat. Energy*, 2023, **8**, 1126–1136.
15 H. Seo, M. P. Nitzsche and T. A. Hatton, *Acc. Chem. Res.*, 2023, **56**, 3153–3164.
16 Y. Guo, M. Massen-Hane, G. Endy and T. A. Hatton, *Adv. Mater.*, 2024, **36**, 2407567.
17 X. Li, X. Zhao, Y. Liu, T. A. Hatton and Y. Liu, *Nat. Energy*, 2022, **7**, 1065–1075.
18 Y. Liu, H.-Z. Ye, K. M. Diederichsen, T. Van Voorhis and T. A. Hatton, *Nat. Commun.*, 2020, **11**, 2278.
19 M. Abdinejad, H. Seo, M. E. L. M. Hane and T. A. Hatton, *Angew. Chem., Int. Ed. Engl.*, 2024, **63**, e202412229.
20 S. Liu, J. Zhang, F. Li, J. P. Edwards, Y. C. Xiao, D. Kim, P. Papangelakis, J. Kim, D. Elder, P. De Luna, M. Fan, G. Lee, R. K. Miao, T. Ghosh, Y. Yan, Y. Chen, Y. Zhao, Z. Guo, C. Tian, P. Li, Y. Xu, E. H. Sargent and D. Sinton, *Energy Environ. Sci.*, 2024, **17**, 1266–1278.
21 Y. Xu, S. Liu, J. P. Edwards, Y. C. Xiao, Y. Zhao, R. K. Miao, M. Fan, Y. Chen, J. E. Huang, E. H. Sargent and D. Sinton, *Joule*, 2023, **7**, 2107–2117.
22 T. Liu, Y. Wang, Y. Wu, W. Jiang, Y. Deng, Q. Li, C. Lan, Z. Zhao, L. Zhu, D. Yang, T. Noël and H. Xie, *Nat. Commun.*, 2024, **15**, 10920.
23 A. Prajapati, R. Sartape, T. Rojas, N. K. Dandu, P. Dhakal, A. S. Thorat, J. Xie, I. Bessa, M. T. Galante, M. H. S. Andrade, R. T. Somich, M. V. Rebouças, G. T. Hutras, N. Diniz, A. T. Ngo, J. Shah and M. R. Singh, *Energy Environ. Sci.*, 2022, **15**, 680–692.
24 P. Zhu, Z.-Y. Wu, A. Elgazzar, C. Dong, T.-U. Wi, F.-Y. Chen, Y. Xia, Y. Feng, M. Shakouri, J. Y. Kim, Z. Fang, T. A. Hatton and H. Wang, *Nature*, 2023, **618**, 959–966.
25 I. A. Digdaya, I. Sullivan, M. Lin, L. Han, W.-H. Cheng, H. A. Atwater and C. Xiang, *Nat. Commun.*, 2020, **11**, 4412.
26 M. D. Eisaman, K. Parajuly, A. Tuganov, C. Eldershaw, N. Chang and K. A. Littau, *Energy Environ. Sci.*, 2012, **5**, 7346–7352.
27 S. Stucki, A. Schuler and M. Constantinescu, *Int. J. Hydrogen Energy*, 1995, **20**, 653–663.
28 S. Matz, B. P. Setzler, C. M. Weiss, L. Shi, S. Gottesfeld and Y. Yan, *J. Electrochem. Soc.*, 2021, **168**, 014501.
29 Q. Shu, M. Haug, M. Tedesco, P. Kuntke and H. V. M. Hamelers, *Environ. Sci. Technol.*, 2022, **56**, 11559–11566.